A Parametric Study of the Performance of Heat Recovery Wheels in HVAC System

Eng. Ghassan J.Softah
Mechanical Engineering Department, Umm Al-Qura University
Makkah – Saudi Arabia
*Gjs_1982@hotmail.com

دراسة حدودية لأداء حلقة حفظ الحرارة في أنظمة التكييف

م. غسان جميل حسن صفطة

ملخص:

تعتبر "عجلة استرجاع الحرارة" عنصراً أساسياً في أنظمة ترشيد الطاقة التي تستخدم في شبكات التكييف للمباني التجارية . وهي عبارة عن عجلة دائرية نفاذية ذات كتلة تخزينية مغلفة بغلاف صلب، تتحرك بحيث تتعارض بشكل متقطع بين المائعين الحار والبارد. يتم تحريك العجلة بمحرك كهربائي بسرعة منخفضة بحيث يمر كل من الهواء الراجع والهواء النقي بالتناوب من خلال أجزاء العجلة. في هذا البحث تم إجراء دراسة حسابية لأهم العوامل المؤثرة في أداء "عجلة استرجاع الحرارة" في ظروف تشغيل مختلفة (حالة الدخول، ومسار تدفق المائع، والمعدن المصنع منه العجلة) في محاولة إلى الوصول لأفضل أداء. كانت نتائج الدراسة الحالية واعدة جداً.

Abstract:

The heat wheel is a key component in solid-energy systems that can be used in commercial building air-conditioning-systems in order to achieve energy savings. Rotary wheel-recovery consists of a rotor with permeable storage mass fitted in a casing that operates intermittently between a hot and a cold fluid. A unique advantage of rotary wheels is the capability of recovering sensible heat. At present, the analysis of the behavior of air handling units based on heat recovery wheels is a complex task to be done by a design engineer. In this work, a computational study of heat recovery wheels is carried out for different operating conditions (inlet state, flow path) to investigate the most effective parameters. The performance of the recovery wheel is evaluated by modeling a representative channel by a commercial software-package (ANSYS-FLUENT).Thus, present results can be taken in great confidence.

1. Introduction

1.1 Background

The waste energy is one of the major global concerns in all science disciplines especially engineering. Also, when designing and applying specific conditions on certain areas such as health facilities, industrial manufactories and laboratories and in order to fulfill their requirements, a massive amount of energy is wasted. The importance of energy saving is manifest on emission levels and energy cost. One of the energy systems where energy saving is implemented is the boilers. The steam-generating boiler's roots go back to the late 1700s with the development of the kettle-type boiler, which simply boiled water into steam. The water was placed over a fire box and then boiled into steam. It was not until around 1867, with the development of the convection boiler that the steam-generating industry began. Another type is air preheaters. The first **Ljungström Air Preheater** was introduced in 1920, and was used for heat exchange in a coal factory. Heat Recovery wheels have been used widely and commercially in order to achieve important energy savings. The rotary wheel recovery consists of a rotor with a permeable storage mass fitted in its casing which operates intermittently between a hot and a cold fluid. The rotor is driven by a motor so that the exhaust air and the fresh air are alternately passed through each section. The rotor speed is normally low (3-15 *rpm*).

At present, the analysis of the behavior of air handling units based on desiccant wheels is a complex task to be designed by a design engineer. It is difficult to develop a simple model that can represent the behavior of commercialized wheels with predetermined accuracy. This study focuses on the "Heating, Ventilating and Air-Conditioning" (HVAC) system requirements to serve a building with 100% fresh air. In order to meet this condition, a major concern regarding energy efficiency becomes vital.

1.2 Present Investigation

In the present investigation, a computational study of heat recovery wheels is carried out on different materials and shapes to investigate the most effective parameters. The performance of the heat recovery wheel is evaluated by modeling a representative channel using a commercial software-package (*ANSYS-FLUENT*). A parametric study is conducted to investigate the influence of different parameters on heat transfer.

Nomenclature

Symbol	Description
A	Heat flow cross-area (m^2)
A_w	Cross-area of matrix (m^2)
B_w	Length of the surface through which heat transfers (m)
C_p	Specific heat at constant pressure (J/(kg ^oC))
C	Thermal capacity rate of flow stream (J/(s ^oC))
C_r	ratio of heat capacity of the matrix to the minimum air heat capacity rate in a rotary air-to-air heat exchanger
D	Inner diameter of the circular tube on one side estimated by all the free-flow flute (m)
d	Diameter of flute (m)
G_k	Production of turbulence kinetic energy
h	Convective heat transfer coefficient of fluid flow (W/(m^2 ^oC))
k	Turbulence generation
k_{eff}	The effective thermal conductivity
k_t	Turbulent thermal conductivity
L	Length of heat wheel (m)
$\dot{m}$	Mass flow rate (kg/s)
M	Mass (kg)
Nu	Nusselt number
Pr	Prandtl number
$\dot{Q}$	Heat transfer rate on the whole cross-area (J/s)
q''	Heat flux (w)
$Ratio$	Ratio of minimum to maximum air heat capacity rates in an air-to-air heat exchanger
R	Heat transfer resistance (m^2 ^oC/W)
Re	Reynolds number
S_h	Volumetric heat source
S	Modulus of the mean rate-of-strain tensor
T	Temperature (K)
U	Total heat transfer coefficient (W/(m^2 ^oC))
$\overline{u^2}$	Normal Reynolds stress
v	Velocity of airflow (m/s)
Greek Letters	
ε_{cf}	Effectiveness of counter flow heat exchanger
λ	Coefficient of bulk viscosity
μ	Absolute viscosity coefficient (kg/(m s))
ϕ	Rotational frequency (revolution per second)
ρ	Density (kg/m^3)
$(\tau)_{eff}$	The deviatoric stress tensor

ν	Kinematic viscosity coefficient (m^2/s)
Superscripts	
C	Cold fluid side of heat exchanger
E	The total energy
F	Fluid
H	Hot fluid side of heat exchanger
W	Wheel matrix
Subscripts	
Hy	Hydraulic
In	Inlet
Max	Maximum value
Min	Minimum value
Out	Outlet
Abbreviations	
AHU	Air handling unit
ASHRAE	American Society of Heating, Refrigerating and Air Conditioning Engineers
CFC	Chlorofluorocarbons
HVAC	Heating, ventilation and air conditioning
NTU	Number of transfer unit

2. Previous Investigations

The design of (HVAC) systems for thermal comfort requires increasing attention, especially matters arising from recent regulations and standards on ventilation [1].The optimum level of indoor temperature is desired to be reached and maintained to ensure a comfortable and healthy environment. Wheel cooling systems have advantages in environmental-conscious operation. As stated by Perez-Lombard et al, [2] building energy consumption has increased as a result of economic growth, expansion of building sectors and spread of heating, ventilation and air conditioning (HVAC) system. Since buildings have a long life span, 50 years or more conserving the energy strategies strictly have stressed on energy loss recovery in buildings[3]. From the reviewed literatures, it can be said that a large amount of energy is lost due to heating, air-conditioning and ventilation. It is thus very important to recover as much as possible this energy by adopting heat or energy recovery systems for building applications. Heat recovery technology offers optimal solutions: using fresh air, better climate control and improving energy utilization efficiency [4].The major advantages of heat recovery wheel are [13]:

1. The system significant electrical power savings, especially where thermal energy sources are easily available.
2. Chlorofluorocarbons (CFCs) free; thus, the system is environmentally friendly.
3. Construction and maintenance are simple.

Because of these advantages, much of the effort has been devoted to research and application of heat recovery wheel components, especially desiccant wheels [3–11]. Heat recovery term is referring to an air-to-air heat or energy recovery system which is defined as the process of recovering energy (heat/mass) from a stream at a high temperature to a low temperature stream that is effective and economical to run [12]. On the other hand, heat conservation [13] defines that heat or energy recovery system as any device that removes in terms of extracts, recovers or salvages heat or mass from one air stream and transfers it to another air stream. This means that the energy that would otherwise be lost is used to heat the incoming air, helping to maintain a comfortable temperature. The optimum temperature and humidity range for human comfort is presented by ASHRAE [2]. In addition, the forced ventilation also has become necessary because the air tightness of buildings has been increasing. *Ge et al.* [14] reviewed the literatures on mathematical models for the rotary wheel and classified the models according to the modeling types of the heat and mass transfer between the air in air-channel and the wheel-wall. Also, there are studies that concentrated on the potential use of heat recovery wheel systems in various locations in the USA and Europe [15–18].

3. System Description

3.1 HVAC System

Figure1 shows a typical heat recovery system installed in ventilation system. In the core, the fresh air stream is automatically preheated or pre-cooled (depending on the season) by the exhausted air and distributed to the interior part of the building. The outgoing and incoming air passes next to each other but do not mix in the heat wheel.

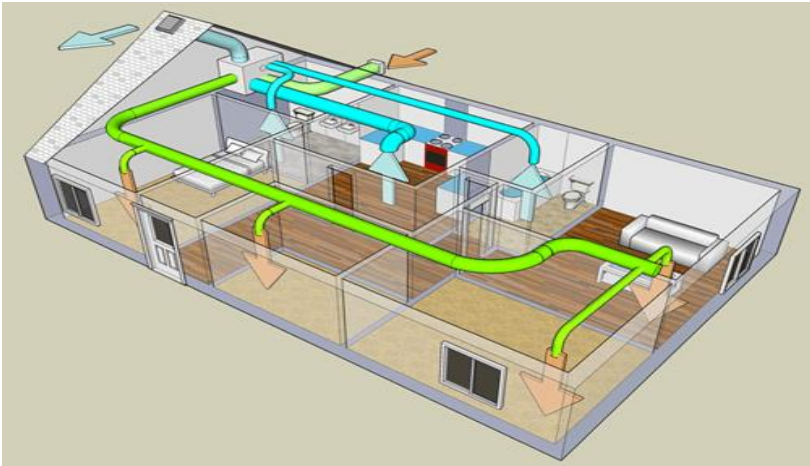

Fig.1 Heat recovery system [12]

3.2 Heat Recovery Wheel

A thermal wheel consists of a circular matrix of heat-absorbing material (Fig. 2), which is slowly rotated within the supply and exhaust air streams of an air

handling system. As the thermal wheel rotates, heat is picked up from the exhaust air stream in one-half of the rotation, and given up to the fresh air stream in the other half of the rotation. Thus, waste heat energy from the exhaust air stream is transferred to the matrix material and then from the matrix material to the fresh air stream (Fig.2), raising the temperature of the supply air stream by an amount proportional to the temperature differential between air streams, or 'thermal gradient', and depending upon the efficiency of the device. Heat exchange is most efficient when the streams flow in opposite directions (counter flow), since this causes a favorable temperature gradient across the thickness of the wheel. The principle of course works in reverse and the energy can be recovered to the supply air stream if so desired and the temperature differential allows.

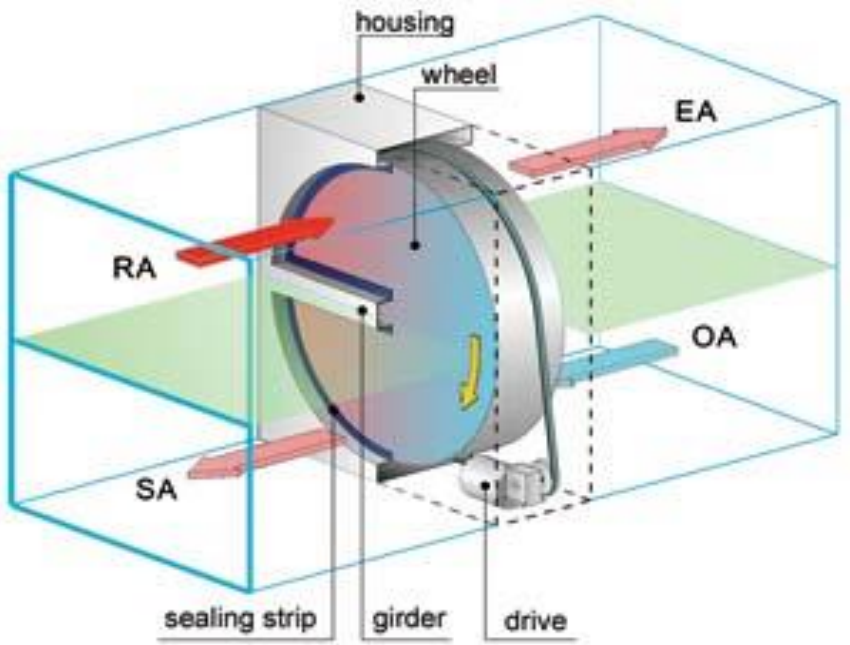

Fig.2Heat recovery wheel [7]

Because of the nature of thermal wheels in the way that heat is transferred from the exhaust air-stream to the supply air-stream without having to pass directly through or via an exchange medium, the gross efficiencies are usually much higher than that of any other air-side heat recovery system.

3.3 Present Work

In this work, a numerical model is used to study and discuss the performance of a cooling system in terms of heat transfer efficiency. The commercial codes *ANSYS-Fluent13* were utilized to carry out the investigation. The investigated component of the heat conservation wheel has the cross-sectional shape of quadrangle, lozenge and sinusoidal shape with four different materials: steel, aluminum, nickel and copper at three different Reynolds numbers.

4. Mathematical Model & Numerical Treatment

4.1 Development of the Mathematical Model

For numerical analysis, it is assumed that the flow is incompressible, unidimensional. Thermal properties of the fluid (such as specific heat, thermal conductivity, density) are assumed to have bulk average values and be uniform at any cross-section. Mass flow rate is constant. Heat transfer is axial to the flow direction. Based on these assumptions, differential equations relating the fluid and matrix temperatures can be derived from the energy balance equation applied to a unit axial element *dz* through the heat wheel control volume. In what follows, we denote by *T* the temperature of fluid and the matrix which is a function of time t and distance *z*,*T=T(t,z)*.

The starting point is the energy balance equation given in the following form:

$$\dot{Q}_{in} + \dot{W} + q''_{w-f} = \dot{Q}_{out} + \left(\frac{\partial E}{\partial t}\right)_{CV} \quad (4.1)$$

Where $\dot{Q}_{in}$ is the energy-input rate with

$$\dot{Q}_{in} = [m.(e + Pv)]_{in} = [m.(KE + PE + u + Pv)]_{in}$$

Our analysis is based on Eq. (4.1) considered in the one-dimensional approximation. Heat convection and heat conduction are analyzed here in the fluid direction over the control volume of (a) each fluid airflow within cross-areas A_{f-h} and A_{f-c} and (b) the wheel matrix within cross-area A_w. In (Fig. 3), we present the diagram for model simplification and provide all necessary details of our definition of the control volume element definition.

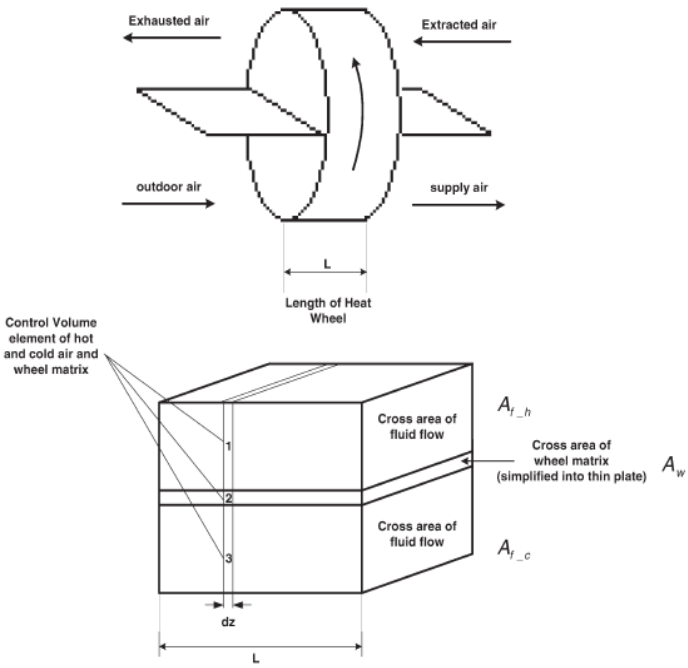

Fig.3 Diagram of thermal model simplification and control volume element definition. [18]

Eq. (4.1) for control volume elements of the extracted air was used. (Fig. 3) illustrates our approach in greater details. In particular, for the control volume elements presented in (Fig. 4) we have the following relationships (written for the extracted air, the wheel matrix and the supply air respectively):

$$\dot{Q}_{f-h,z+dz} - \left(\lambda_{f_h} . A_{f_h} \frac{\partial T_{f_h}}{\partial z} \Big|_{z+dz} - \lambda_{f_h} . A_{f_h} \frac{\partial T_{f_h}}{\partial z} \Big|_{z} \right) = \dot{Q}_{f-h,z} + q''_{f_h-w} + \frac{\partial \dot{M}_{f_h}}{\partial z}, \qquad (4.2)$$

$$\frac{\partial \dot{M}_{w}}{\partial z} = q''_{f_h-w} - q''_{w-f_c} + \left[\lambda_w . A_w \frac{\partial T_w}{\partial z} \Big|_{z+dz} - \lambda_w . A_w \frac{\partial T_w}{\partial z} \Big|_{z} \right] \qquad (4.3)$$

$$\dot{Q}_{f_c} + q''_{w-f_c} + \left(\lambda_{f_c} . A_{f_c} \frac{\partial T_{f_c}}{\partial z} \Big|_{z+dz} \right) - \lambda_{f_c} . A_{f_c} \frac{\partial T_{f_c}}{\partial z} \Big|_{z} = \dot{Q}_{f_c,z+dz} + \frac{\partial \dot{M}_{f_c}}{\partial z} \qquad (4.4)$$

In (4.2)–(4.4), for both $\dot{Q}_{f_h}$ and $\dot{Q}_{f_c}$ we have:

$$\dot{Q} = \dot{m}h = \dot{m}c_p \Delta T \qquad (4.5)$$

Furthermore, we have $KE = 0$, $PE = 0$ in $\dot{Q}$ and $u + Pv = h$,

$$\frac{\partial \dot{M}}{\partial z} = \dot{M}h = \dot{M}c_p \frac{\partial T}{\partial z} \qquad (4.6)$$

$$q'' = U . B_w (T_w - T_f) dz \qquad (4.7)$$

For both E_{f_h}, E_{f_c}, E_w and q''_{f_h-w}, q''_{w-f_c}

$$\lambda . A \frac{\partial T}{\partial z} \Big|_{z+dz} - \lambda . A \frac{\partial T}{\partial z} \Big|_{z} = \left[\lambda . A \frac{\partial T}{\partial z} \right]_{z}^{z+dz} = \lambda . A \int_{z}^{z+dz} \left(\frac{\partial T}{\partial z} \right) d\xi \qquad (4.8)$$

By substituting Eqs. (4.5)–(4.8) for Eqs. (4.2)–(4.4), we obtain a set of three equations:

- For the extracted air:

$$\dot{m}_{f_h} h_{f_h,z+dz} - \lambda_{f_h} . A_{f_h} \int_{z}^{z+dz} \left(\frac{\partial T_{f_h}}{\partial z} \right) d\xi = \dot{m}_{f_h} h_{f_h,z} + \int_{z}^{z+dz} B_w U (T_{f_h} - T_w) d\xi + \frac{\partial}{\partial z} \int_{z}^{z+dz} (A_{f_h} \rho_{f_h} h_{f_h}) d\xi \qquad (4.9)$$

- For the supply air:

$$\dot{m}_{f_c} h_{f_c,z} + \int_{z}^{z+dz} B_w U (T_w - T_{f_c}) d\xi + \lambda_{f_c} . A_{f_c} \int_{z}^{z+dz} \left(\frac{\partial T}{\partial z} \right) d\xi = \dot{m}_{f_c} h_{f_c,z+dz} + \frac{\partial}{\partial z} \int_{z}^{z+dz} (A_{f_c} \rho_{f_c} h_{f_c}) d\xi \qquad (4.10)$$

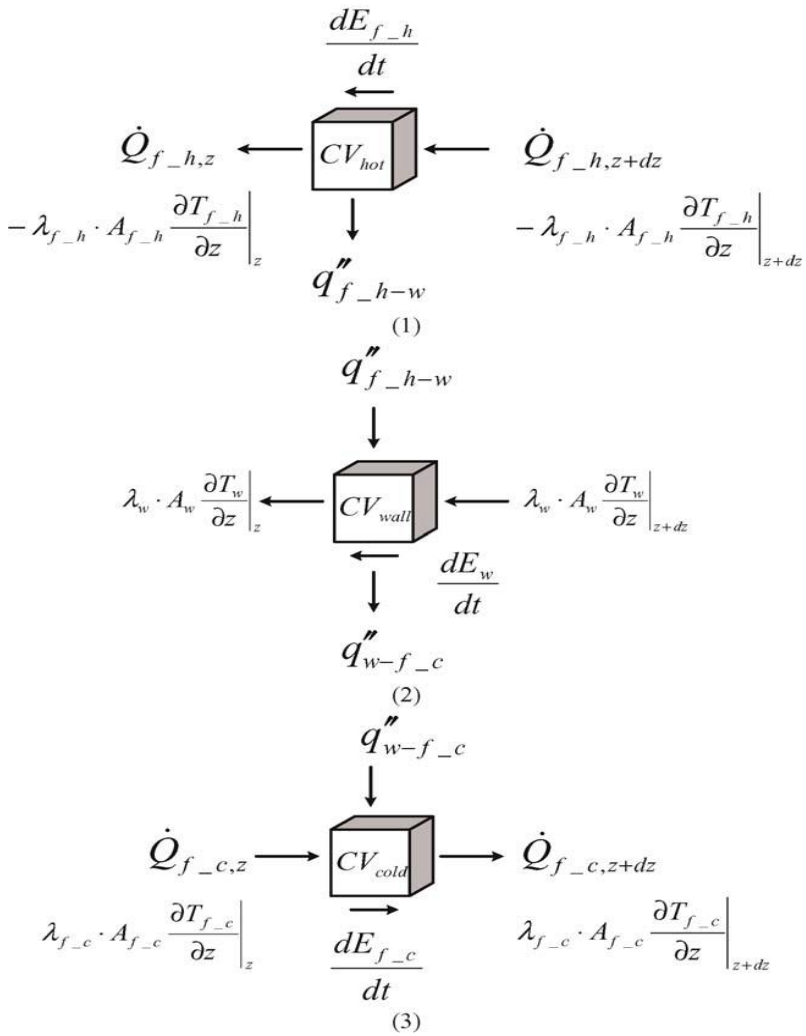

Fig.4 Schematic diagram describing the energy balance analysis for a control volume of: (1) extracted air; (2) wheel matrix; (3) supply air. [18]

❖ For the wheel matrix:

$$M_w C_{p,w} \frac{\partial T_w}{\partial t} = UB_w L(T_{fh} - T_w) - UB_w L(T_w - T_{fh}) + \lambda_w . A_w . L \left[\frac{\partial^2 T_w}{\partial z^2} \right] \qquad (4.11)$$

In the context of (4.9)–(4.11) we note that

$$\dot{m}_{f\ h} h_{f\ h,z+dz} - \dot{m}_{f\ h} h_{f\ h,z} = [\dot{m}_{f\ h} h_{f\ h,z+dz}]_z^{z+dz} = \dot{m}_{f\ h} \int \frac{\partial h}{\partial z} d\xi, \qquad (4.12)$$

$$\dot{m}_{f\ c} h_{f\ c,z+dz} - \dot{m}_{f\ c} h_{f\ c,z} = [\dot{m}_{f\ c} h_{f\ c,z+dz}]_z^{z+dz} = \dot{m}_{f\ c} \int \frac{\partial h}{\partial z} d\xi, \qquad (4.13)$$

$$h = C_p(T - T_{ref}) \qquad (4.14)$$

4.2 Turbulence Modeling - Realizable k- ε turbulence model

The realizable ***k - ε***turbulence model was used in the present study. The realizable ***k- ε*** model differs from the standard ***k- ε*** model in two important ways:

- The realizable ***k- ε*** model contains an alternative formulation for the turbulent viscosity.
- A modified transport equation for the dissipation rate,***ε***, has been derived from an exact equation for the transport of the mean-square vorticity fluctuation.

For further details about the realizable ***k- ε*** turbulence model, one may refer to [21].

5.Computational Aspects and Test cases

5.1 Overview

In this section the computational aspects of the solution of the governing equations that were presented in the previous section are shown. Moreover, the examined test cases are also shown. As mentioned in Sec.3 above, the conservation wheel contains flow passages that form a matrix of similar channels. The present study concerns the flow and thermal fields through these channels. As these channels are similar, only one complete channel is considered. The flow was treated as steady without the effect of wheel rotation. The flow in the channel was kept hotter than the surroundings. Due to the nature of the AHU system, the channel flow was treated as turbulent. The realized ***k-ε***model (Sec.4) was adapted to solve the turbulent flow.

5.2 Computational Aspects

5.2.1 Computational Domain and Boundary Conditions

The computational domain, for all test cases, is a three dimensional (3-D) domain, (Fig. 5).

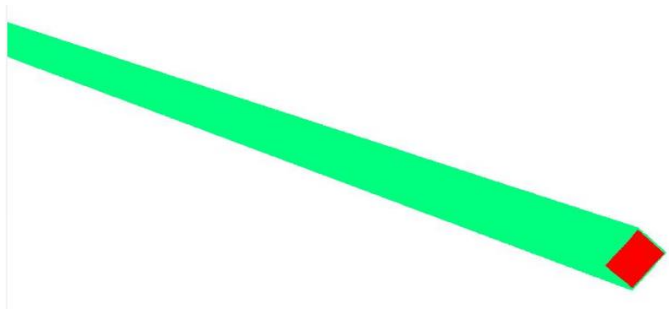

Fig.5Computational domain

The ratio between the length of the channel and its hydraulic diameter (L/D) is (33.33). Typically, in *ANSYS-FLUENT* three types of boundary conditions that can be listed as:

- **Inlet boundary condition:** inlet uniform velocity is specified at the entrance of the channel. According to ASHRAE standards, the inlet temperature was taken as 319 K. This temperature value represents the annual average ambient temperature in Makkah.
- **Outlet boundary condition**: The function of "Pressure outlet" in *ANSYS-FLUENT*is used and outlet temperature 300 K**.**
- **Wall boundary condition:** the walls of the channel was treated as smooth solid walls. The no-penetration and no-sliding conditions were applied at the channel walls. The temperature at the inner surface of the walls was kept at 309K for all test cases. This makes a temperature difference of 10K between the inlet flow and the inner surface. This difference value was recommended in the literature [18]**.** The wall material changes depending on the test case (Sec.5.3).

5.2.2 Computational Grid (Mesh)

Due to the complexity of the geometry of the channels, the computational domain was discretized using unstructured grids. This type of grids usually guarantees the flexibility to generate enough computational points in locations of severe gradients. Unstructured grids adopt themselves easily to irregular geometries with minimum programmer's effort. The computational domain was covered by tetrahedral-shaped elements, (Fig. 6). The grid is very fine next to the solid boundary. The dimensionless distance between the wall and first computational point $y^+ \approx 2$. y^+ is calculated as

$$y^+ = \frac{[illegible]}{[illegible]} \quad (5.1)$$

Where, y is the distance to the first point off the wall, υ is the kinematic viscosity, u_τ is the friction velocity.

$u_\tau = \sqrt{\frac{\tau}{\rho}}$, τ is the wall shear stress and ρ is the flow density. The value of $y^+ = 2$ ensures the resolution of the complex turbulent flow.

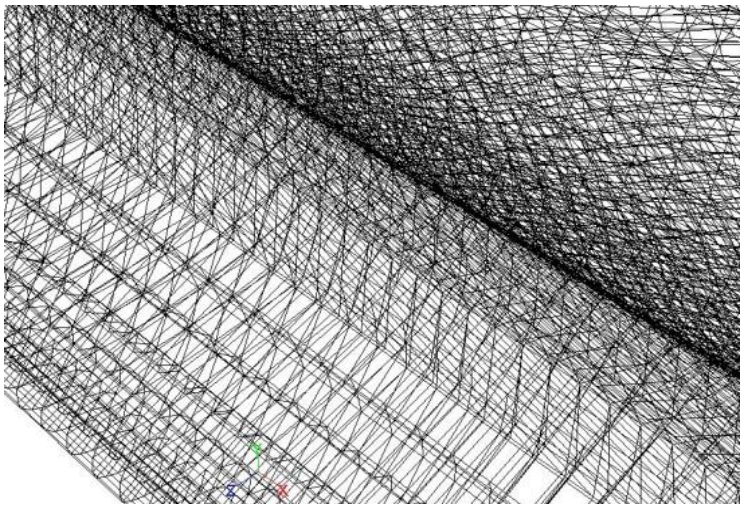

Fig. 6 Enlarged grid structure (sample)

5.2.3 Grid Size and Independency

Careful consideration was paid to ensure the grid-independency of the computational solution. Thus, three grid sizes were used to test the grid-independency, namely: 100,000, 150,000 and 200,000 elements (cells). The results of both the flow and thermal fields show that the difference between the results of the middle and third grids is in the range of 1-2 %. The grid of (200,000) needs a lot of computer run-time in *ANSYS-FLUENT*. Thus, the second grid size (150,000) was used for all the test cases to reduce running time.

5.2.4 Numerical Method

In *ANSYS-FLUENT*, simple algorithm (Semi-implicit method for pressure – linked equations) was employed to solve for the velocity and pressure fields. Each equation of the momentum and energy was solved by "first-order upwind" scheme. The "standard wall function" was used as the near-wall treatment technique in the turbulence model. The solution continues until the numerical residual (error) of all quantities get below 10^{-5}.

5.3 Test cases

A parametric study was carried out to obtain the best case for optimum operation. The parametric study covered the shape of the channel cross-section, the wall material, and the flow Reynolds number. Three cross-sectional shapes were considered, Quadrangle, Lozenge and Sinusoidal. The sinusoidal cross-section is widely used in conservation wheels. It is used here mainly for comparison purposes. The other two shapes are proposed by the author. The Quadrangle shape has good characteristics considering flow and thermal fields. On the other hand, the Lozenge shape has good structural properties. Four materials were tested as walls of the channels, namely: copper, aluminum, nickel and steel. The computations were performed at three values of Reynolds numbers, 1200, 1830 and 2200. This range of Reynolds number is taken, based on the operating conditions Ref. [18]. Seiichi study was based on the Reynolds number of 1830. To demonstrate the effect of Reynolds number in the same operating range, the two other values of 1200 and 2200 were adapted. Reynolds number was ~~is~~ calculated based on inlet velocity and the hydraulic diameter of the channel, *i.e.*

$$Re = \frac{u_{in} d_h}{\upsilon} \quad (5.2)$$

Where u_{in} is the inlet velocity, d_h is the hydraulic diameter, υ is the kinematic viscosity. This combination of parameters lead to thirty six (36) test case. (Table.1) shows a summary of studied test cases.

Shape	Material	Reynolds No.
Quadrangle	Copper	1200
	Aluminum	1830
	Nickel	
	Steel	2200
Lozenge	Copper	1200
	Aluminum	1830
	Nickel	
	Steel	2200
Sinusoidal	Copper	1200
	Aluminum	1830
	Nickel	
	Steel	2200

Table. 1: Summary of the test case

5.4 Validation of the Work

In the present work, the present numerical results compare very well to the experimental data obtained by others [18] as shown in (Fig.7) for the temperature contours. Generally, the same trend of temperature distribution was obtained in both (Fig. 7) and (Fig. 8). More gradient contours appear in (Fig. 8). This may occur due to the secondary flow that was considered by [18] and not considered in the present investigation. Since the present numerical model was effectively validated, the outputs of present study are to be considered with confidence.

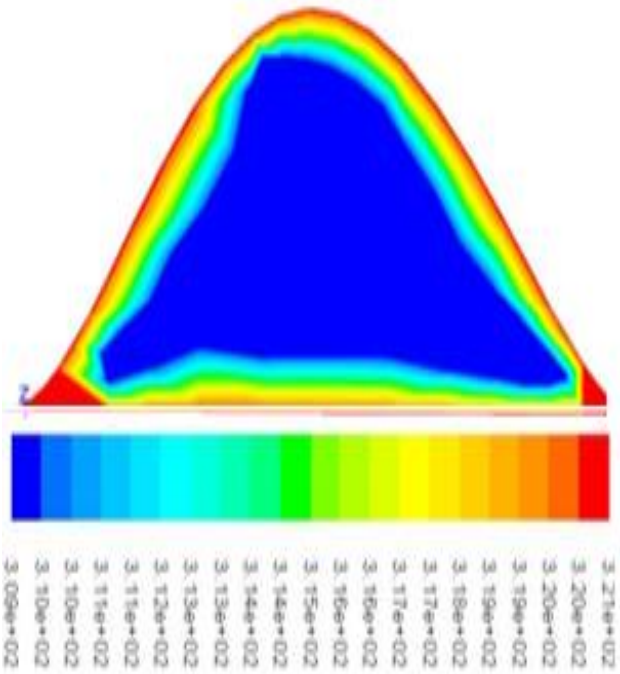

Fig. 7Temperature field, cross-sectional view, present computational predictions.

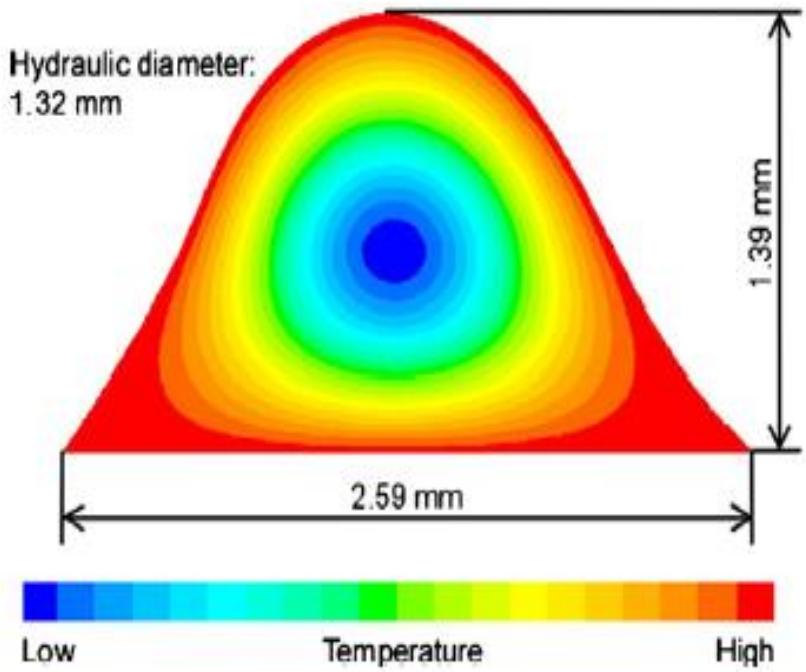

Fig. 8Temperature field, cross-sectional view,
Experimental work [18]

6. Results and Discussions

The results cover both the flow and thermal fields. The flow field concerns the working fluid (air) that transfers heat. Thus, the flow field of the different cases is presented firstly. Then, the thermal field results are presented. Naturally, attention is paid to the thermal field as heat transfer enhancement is the principal goal of the study.

6.1 Flow Field

(Fig. 9) Shows the velocity contours at the entrance and exit of the quadrangle cross-section channel at *R*e = 1830 and aluminum. It is clear from the velocity contours at exit that the flow becomes fully developed before the channel exit and the highest velocity is shown in the middle of cross-section shapes. The same pattern of quadrangle cross-section is repeated typically for lozenge cross-section(Fig. 10) and for sinusoidal cross-section(Fig. 11).

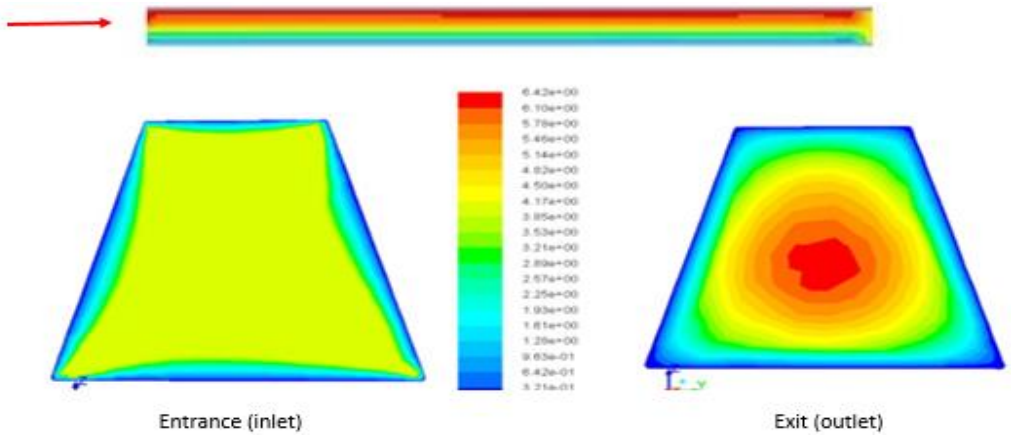

Fig. 9Velocity contours for Quadrangle shape Re= 1830 and Aluminum

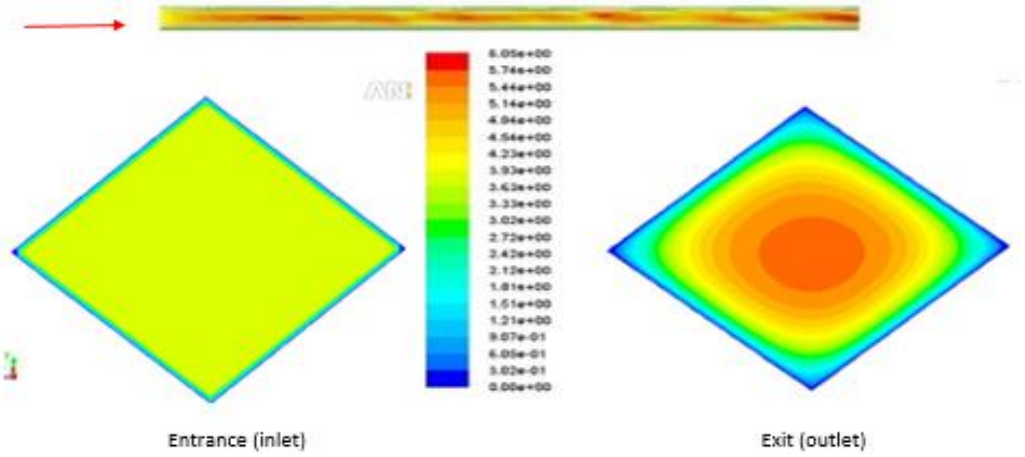

Fig. 10 Velocity contours for Lozenge shape *Re*= 1830 and Aluminum

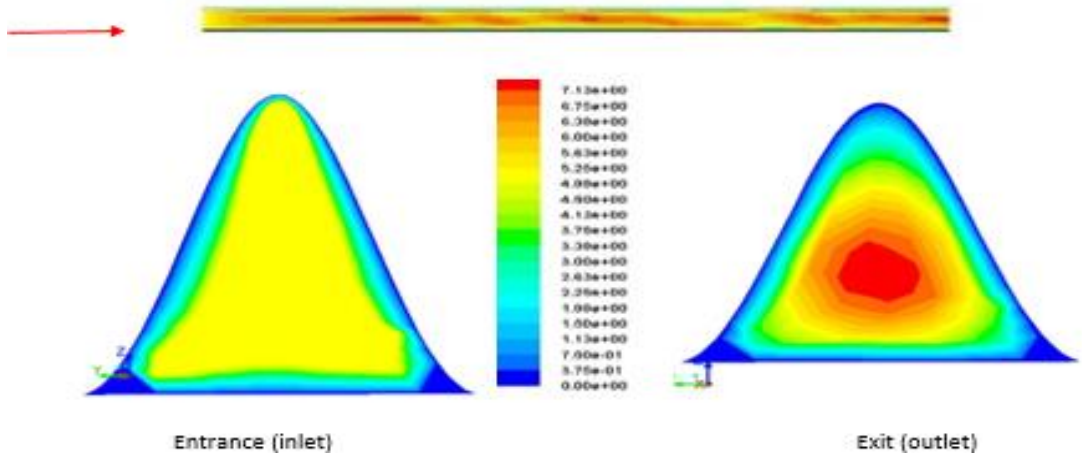

Fig. 11 Velocity contours for Sinusoidal Re= 1830 and Aluminum

This ensures the fully developed nature of the flow inside the channel.

However, the entrance length may change from one case to another. This variation of entrance length affects greatly the thermal field as will be explained in the coming sections.

6.2 Pressure Field

(Fig. 12) shows the pressure distribution along the quadrangle cross-section channel as well as at entrance and exit for *Re*= 1830 and aluminum material.

It is clear from (Fig. 12) that the flow in the channel causes a considerable pressure drop from the entrance to the exit. The same pattern of quadrangle cross-section (Fig. 12) is obtained for lozenge cross-section (Fig. 13) and for sinusoidal cross-section (Fig. 14).

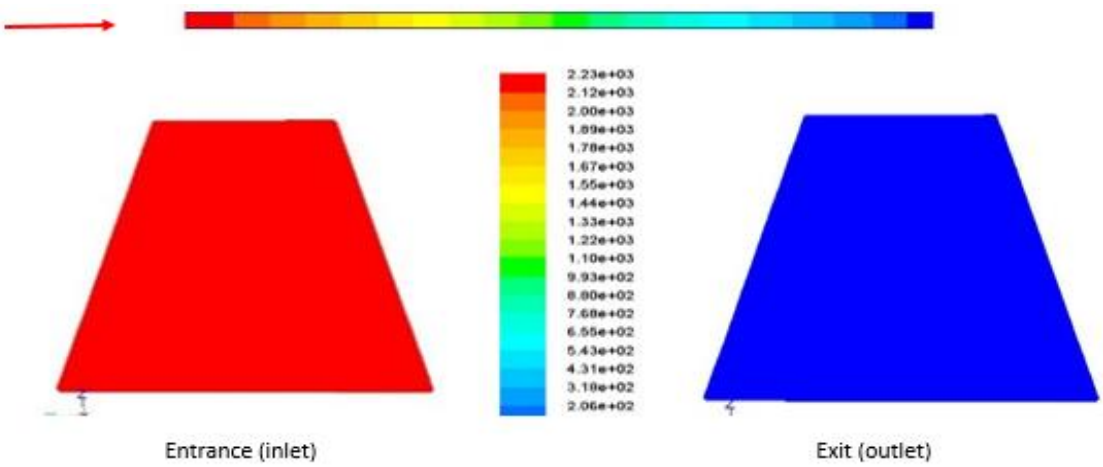

Fig. 12. Pressure Contours Quadrangle shape, Re= 1830 and Aluminum

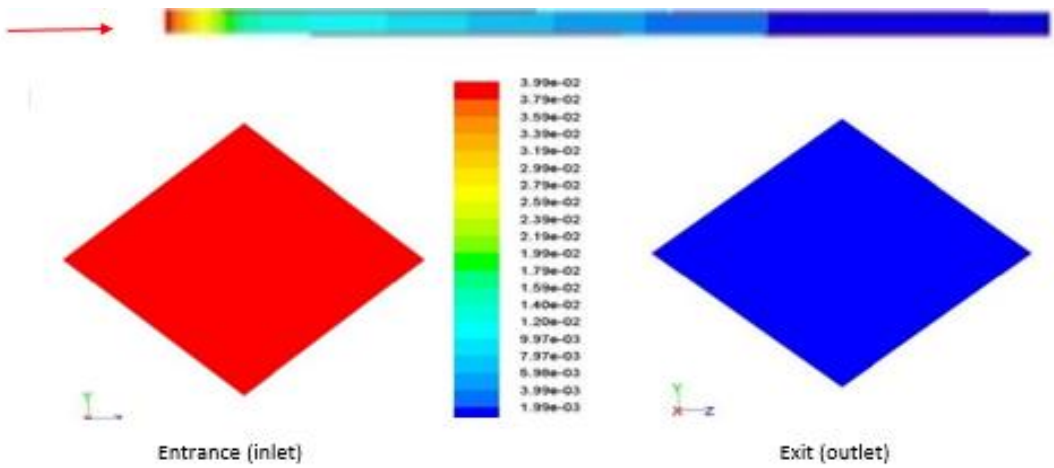

Fig. 13 Pressures ContoursLozenge shapeRe= 1830 and Aluminum

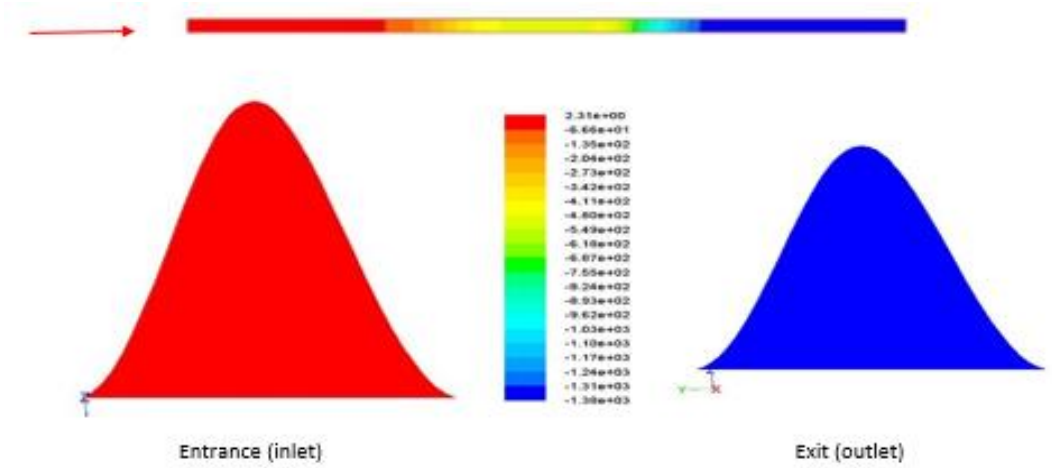

Fig. 14 Pressure Contours for Sinusoidal Re= 1830 and Aluminum

6.3 Thermal Field

To estimate the effect of different parameters on the heat transfer along the channel, a certain criterion should be established. This criterion concerns the different thermal zones along the channel in the stream-wise direction. The length of the channel was divided into three consequent zones; hot, middle and cold. For generality, the lengths of the three zones are normalized by the total length of the channel. Thus, these lengths can be defined from the temperature gradients (color gradients) as shown in (Fig. 15). Apparently, the greater the value of length of cold zone (L_c), the better the heat transfer process is, due to the effectiveness and thermal conductivity of the material.

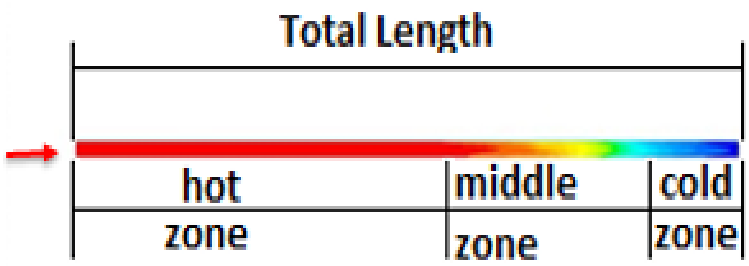

Fig. 15 Thermal zones along the channel length

This criterion was implemented in the present study to determine the combination of parameters that gives the best heat transfer process based on the temperature gradients (color gradients) in each case.

6.3.1 Quadrangle cross-section

(Fig. 16) shows the temperature contours along the channel as well as entrance and exit sections for *Re*= 1830 and aluminum material. It is clear from (Fig.16) that the temperature inside the channel drops from the inlet temperature to the wall temperature well before exiting the channel.

The pattern of temperature contours at entrance and exit of the channel is repeated for all cases. However, the temperature contours along the channel length varies from one case to another depending on the case parameters. (Fig.20) shows the temperature contours along the channel length for all cases.

Based on the results of (Fig. 17), the percentage relative lengths of the thermal zones along the channel for different cases are shown in (Fig. 18).

It is clear from (Fig. 18) that at the same Reynolds number of 1830, the longest cold zone has a percentage of relative length of cold zone (L_c) = 94% and length of hot zone(L_h) =3% for the copper material.

When considering aluminum as the wall material at different values of Reynolds number, the longest cold zone has a percentage relative length of L_c = 95% and L_h = 3% at *Re*= 1200.

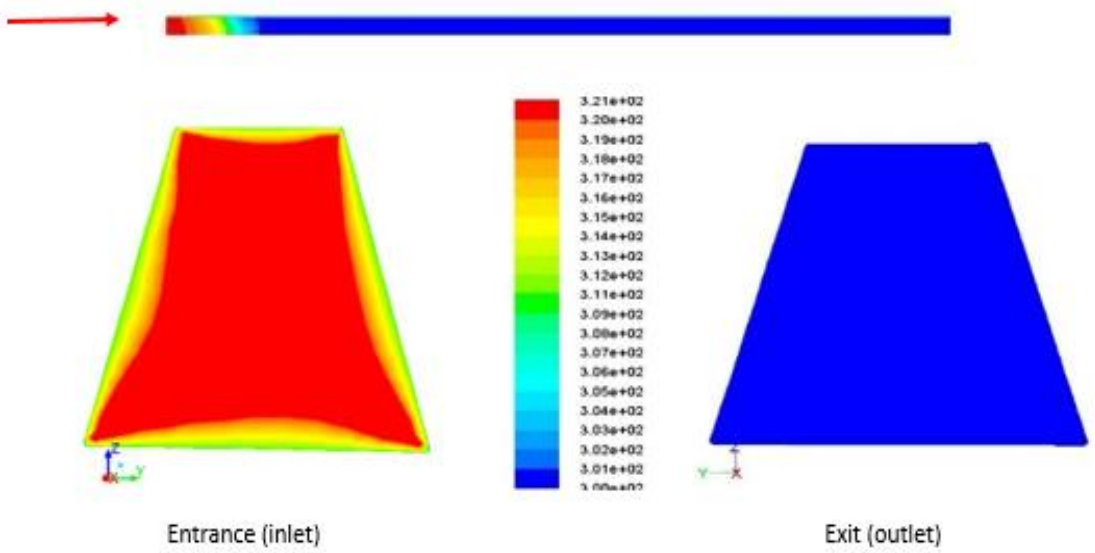

Fig. 16 Temperature Contours Re= 1830, Aluminum material

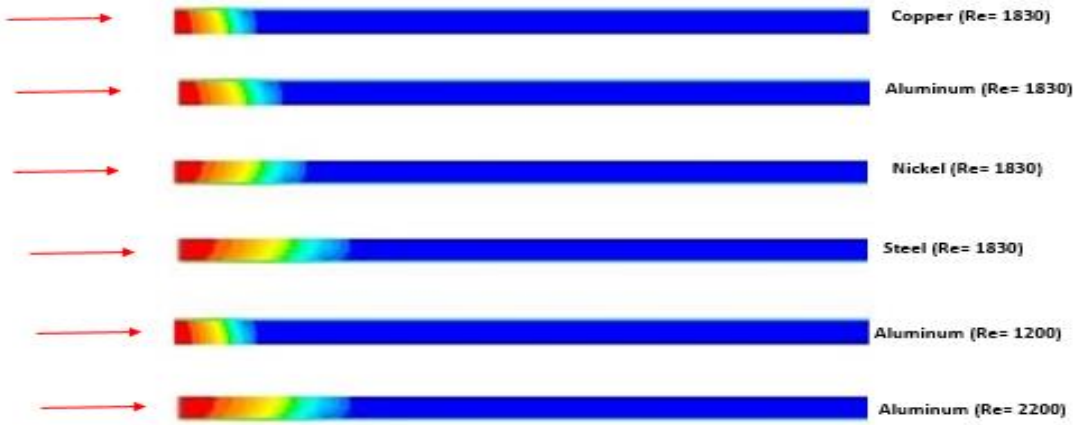

Fig. 17 Temperature Contours for all materials of Quadrangle cross-section

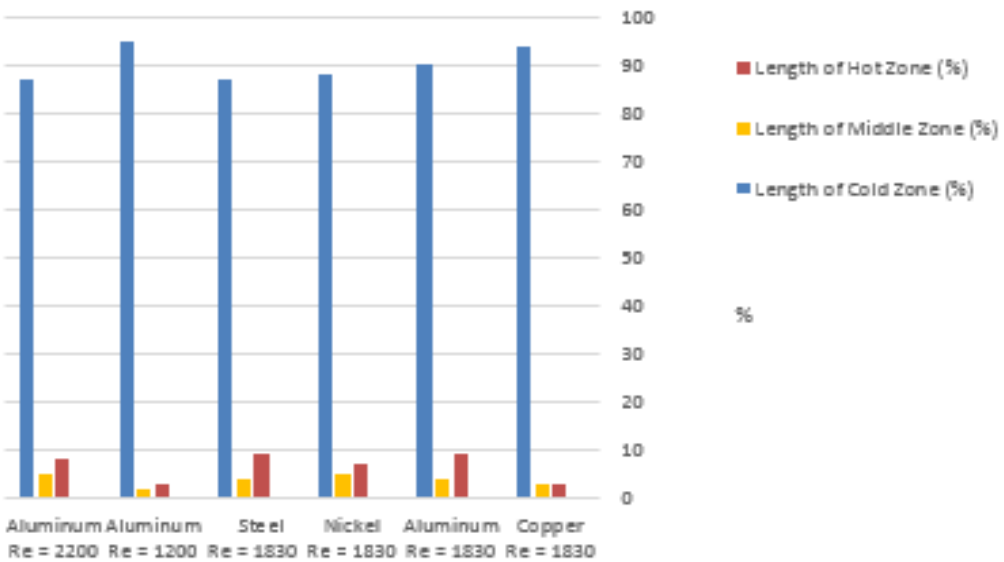

Fig. 18 Bar chart for the Quadrangle shape identifying the three zones

6.3.2 Lozenge cross-section

(Fig. 19) shows that temperature contours along the channel as well as at entrance and exit section for *Re*= 1830 and aluminum material. It is clear from (Fig.19) that the temperature inside the channel drops from the inlet temperature to the wall temperature well before exiting the channel. (Fig.20) shows the temperature contours along the channel length for all cases. Based on the results of (Fig.20), the percentage relative lengths of the thermal zones along the channel for different cases are shown in (Fig. 21). It is clear from (Fig. 21)that at the same Reynolds number of 1830, the longest cold zone has a percentage relative lengths of L_c = 21% and L_h=71% for copper.

When considering aluminum as the wall material at different values of Reynolds number, the longest cold zone has percentage relative lengths L_c = 75% and

L_h = 15% at *Re*= 1200 and with *Re*= 2200 L_c = 30% and L_h = 55%.

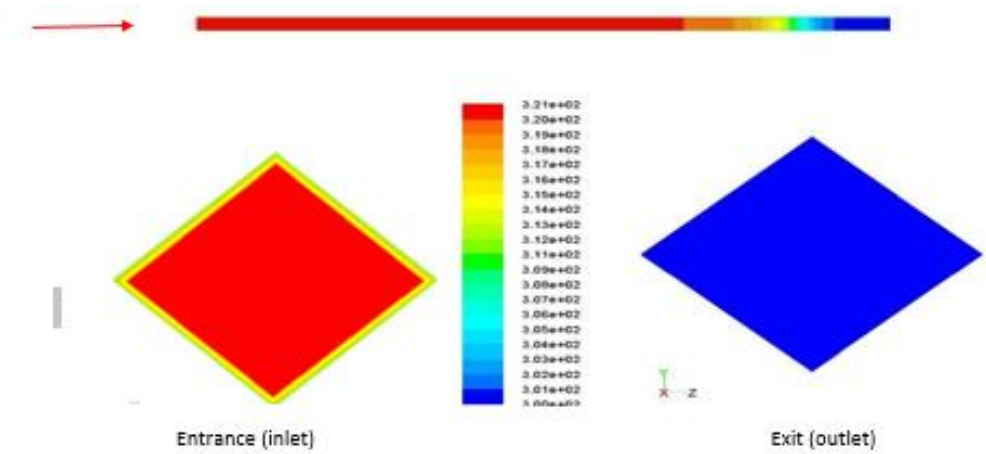

Fig. 19 Temperature Contours Re= 1830, Aluminum material

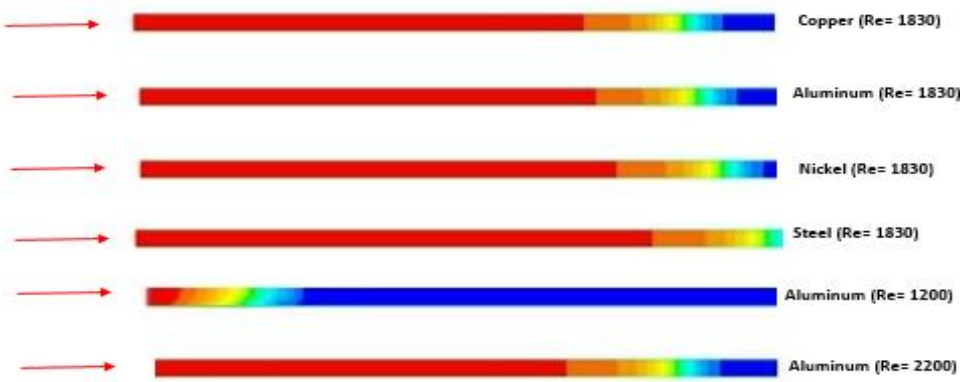

Fig. 20 Temperature Contoursfor all materials of Lozenge cross-section

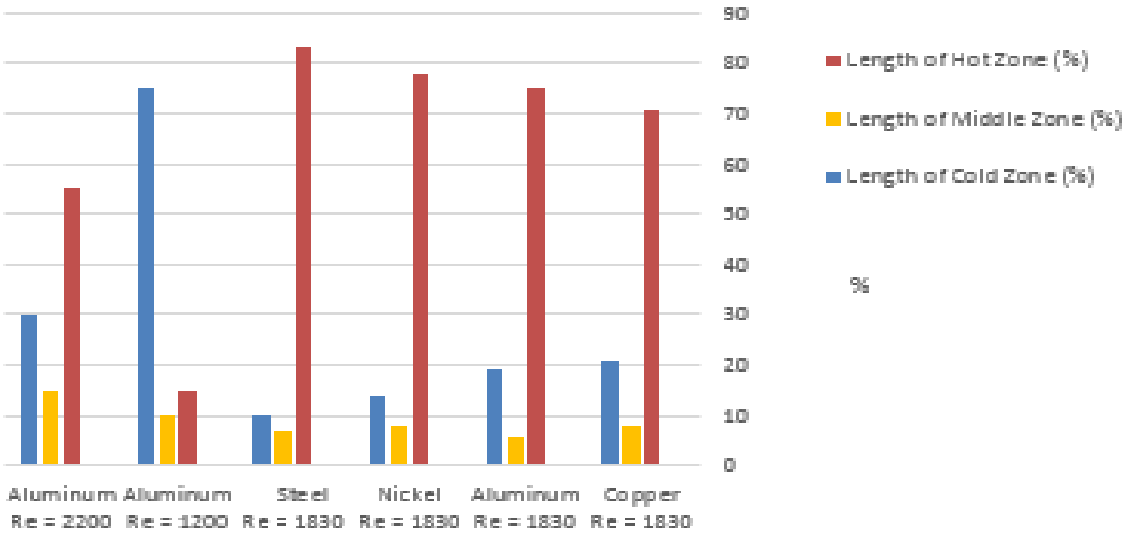

Fig. 21 Bar chart for the Lozenge shape identifying the three zones

6.3.3 Sinusoidal cross-section

Figure22 shows the temperature contours along the channel as well as entrance and exit sections for *Re*= 1830 and aluminum material. It is clear from (Fig. 22) that the temperature inside the channel drops from the inlet temperature to the wall temperature well before exiting the channel. The pattern of temperature contours at entrance and exit of the channel is repeated for all cases. However, the temperature contours along the channel length changes from one case to another depending on the case parameter.

Figure 23 shows the temperature contours along the channel length for all cases. Based on the results of (Fig.23), the percentage relative lengths of the thermal zones along the channel for different cases are shown in (Fig. 24).It is clear from (Fig. 24) that at the same Reynolds number of 1830, the longest cold zone has a percentage relative lengths of L_c = 65% and L_h=18% for copper.

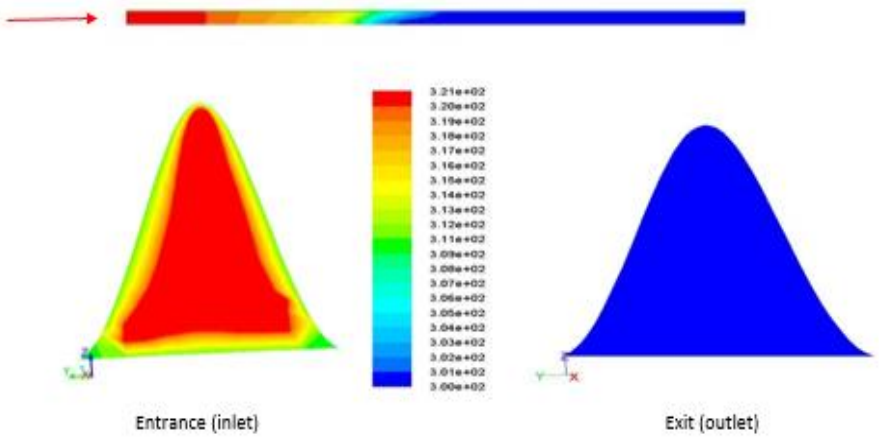

Fig. 22 Temperature Contours Re= 1830, Aluminum material

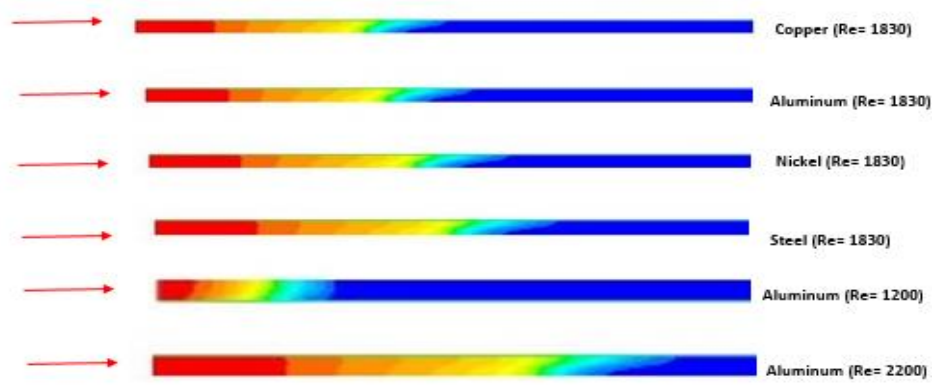

Fig. 23Temperature Contoursfor all materials of Sinusoidal cross-section

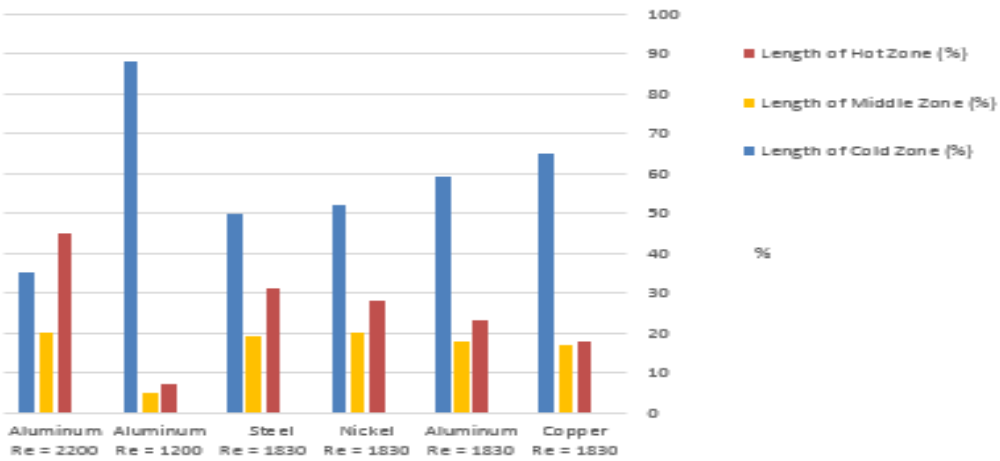

Fig. 24 Bar chart for the Sinusoidal shape identifying the three zones

When considering aluminum as the wall material at different values of Reynolds number, the longest cold zone has percentage relative lengths of L_c = 88% and L_h = 7% at *Re*= 1200 and with *Re*= 2200 L_c = 35% and L_h = 45%.

6.3.4 Overall view of all cases

Based on the results of the previous sections, an overall view of all cases can be demonstrated. Table. 2 illustrates overall results of the percentage relative lengths of all cases.

It is clear that if the Reynolds number increases, the value of L_c is decreases and the better heat transfer process is obtained with lower Reynolds number. In addition, the copper material shows a very good heat transfer performance.

Shape	Material	Length of Hot Zone (%)	Length of Middle Zone (%)	Length of Cold Zone (%)
Quadrangle	Copper Re = 1830	3	3	94
	Aluminum Re = 1830	9	4	90
	Nickel Re = 1830	7	5	88
	Steel Re = 1830	9	4	87
	Aluminum Re = 1200	3	2	95
	Aluminum Re = 2200	8	5	87
Lozenge	Copper Re = 1830	71	8	21
	Aluminum Re = 1830	75	6	19
	Nickel Re = 1830	78	8	14
	Steel Re = 1830	83	7	10
	Aluminum Re = 1200	15	10	75
	Aluminum Re = 2200	55	15	30
Sinusoidal 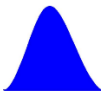	Copper Re = 1830	18	17	65
	Aluminum Re = 1830	23	18	59
	Nickel Re = 1830	28	20	52
	Steel Re = 1830	31	19	50
	Aluminum Re = 1200	7	5	88
	Aluminum Re = 2200	45	20	35

Table 2: Study Results

7. Conclusions

This study aimed to find the best operating parameters to obtain the highest level of thermal heat transfer. The results and discussions of the previous sections lead to the following concluding remarks:

1. The present numerical model and solution scheme were effectively validated. So the outputs of the present study are to be considered with confidence.
2. For the considered range of Reynolds numbers (1200 – 2200), the best thermal performance was noticed for the lowest value of Reynolds number (Re = 1200).

3. The best thermal performance was obtained when the channel cross-section was Quadrangle. The Lozenge shape had the poorest thermal performance.
4. For all cases, the wall materials can be arranged from best to worst as: Copper, Aluminum, Nickel and Steel when considering the thermal performance.

8. Acknowledgements

This work was funded by Umm Al-Qura University and was performed as part of the fulfillment of the Master Degree. Foremost, I would like to express my sincere gratitude to my advisors who guided me through this work: Professor Muhammad Naeem Radhwi and Professor Ahmed Farouk Abdel Gawad, for the continuous support and guidance throughout my master degree study.

9. References

1. Mazzei, P., Minichiello, F., Palma, D., 2002. Desiccant HVAC systems for commercial buildings. Applied Thermal Engineering 22, 545–560.
2. Pérez-Lombard L, Ortiz J, Pout C. A review on buildings energy consumption information. Energy and Buildings 2008;(40):394–8.
3. Wan KKW, Li HWD, Liu D, Lam JC. Future trends of building heating and cooling loads and energy consumption in different climates. Building and Environment 2011;(46):223–34.
4. Shao L, Riffat SB, Gan G. Heat recovery with low pressure loss for natural ventilation. Energy and Buildings 1998;(28):179–84.
5. E.M. Sterling, A. Arundel, T.D. Sterling, Criteria for human exposure to humidity in occupied buildings, ASHRAE Trans. 91 (1) (1985) 611–622.
6. ASHRAE, 2005 ASHRAE Handbook Fundamentals SI Edition, ASHRAE, Atlanta, 2005.
7. Dai, Y.J., Wang, H.F., Zhang, H.F., 2001b. Parameter analysis to improve rotary desiccant dehumidification using a mathematical model. International Journal of Thermal Science 40, 400–408.
8. Ahmed, M.H., Kattab, N.M., Fouad, M., 2005. Evaluation and optimization of solar desiccant wheel performance. Renewable Energy 30, 305–325.
9. Zhang, X.J., Dai, Y.J., Wang, R.Z., 2003. A simulation study of heat and mass transfer in a honeycombed rotary desiccant dehumidifier. Applied Thermal Engineering 23, 989–1003.
10. Zheng, W., Worek, W.M., 1993. Numerical simulation of combined heat and mass transfer process in a rotary dehumidifier. Numerical Heat Transfer Part A 23, 211–232.
11. Harriman III, L.G., 1994. The basics of commercial desiccant systems. Heating/Piping/Air Conditioning,77–85.
12. Riffat SB, Gan G. Determination of effectiveness of heat-pipe heat recovery for naturally-ventilated buildings. Applied Thermal Engineering 1998;(18):121–30.

13. Shurcliff W. Air-to-air heat exchangers for houses. Annual Review Energy 1988;(13):1-2
14. T.S. Ge, Y. Li, R.Z. Wang, Y.J. Dai, A review of the mathematical models for predicting rotary desiccant wheel, Renew. Sustain. Energy 2008. Rev. 12 1485–1528.
15. J.Y. San, S.C. Hsiau, Effect of axial solid heat conduction and mass diffusion in a rotary heat and mass regenerator, Int. J. Heat Mass Transfer 1993. 36 (8) 2051–2059
16. H.M. Henning, T. Erpenbeck, C. Hindenberg, I.S. Santamiria, The potential of solar energy use in desiccant cooling cycles, International Journal of Refrigeration 2001. 24 220–229.
17. P. Mavroudaki, C.B. Beggs, P.A. Sleigh, S.P. Halliday, The potential for solar powered single-stage desiccant cooling in southern Euro, Applied Thermal Engineering 2002. 22 1129–1140.
18. Seiichi Yamaguchi , Kiyoshi Saito Numerical and experimental performance analysis of rotary desiccant wheels Department of Applied Mechanics and Aerospace Engineering, Waseda University, 3-4-1 Okubo, Shinjuku-ku, Tokyo 169-8555, Japan
19. S.P. Halliday, C.B. Beggs, P.A. Sleigh, The use of solar desiccant cooling in the UK: a feasibility study, Applied Thermal Engineering 2002. 22 1327–1338.
20. Zhuang Wu a, Roderick V.N. Melnikb, Finn Borup a Department of Control Engineering, Aalborg University, Fredrik BajersVej 7C, Aalborg, DK-9220, Denmark b Mathematical Modelling and Computational Sciences, Wilfrid Laurier University,1995.
21. Fluent guide manual, 2011.